CrossMark

TECHNICAL ARTICLE

X-ray diffraction and density functional theory studies of $R(Fe_{0.5}Co_{0.5})O_3$ (R = Pr, Nd, Sm, Eu, Gd)

W. Wong-Ng,[1,a] G. Liu,[2] I. Levin,[1] I. Williamson,[3] P. Ackerman,[4] K. R. Talley,[3] J. Martin,[1] K. AlHamdan,[5] W. Badegaish,[5] J. A. Kaduk,[6] and L. Li[3,7]

[1]*Materials Measurement Science Division, National Institute of Standards and Technology, Gaithersburg, Maryland 20899*
[2]*Science Research Institute, China University of Geosciences, Beijing 100083, China*
[3]*Micron School of Materials Science and Engineering, Boise State University, Boise, Idaho 83725*
[4]*Department of Materials Science and Engineering, Carnegie Melon University, Pittsburgh, Pennsylvania 15213*
[5]*Department of Materials Science and Engineering, The Catholic University of America, Washington, DC 20064*
[6]*Department of Chemistry, Illinois Institute of Technology, Chicago, Illinois 60616*
[7]*Center for Advanced Energy Studies, Idaho Falls, Idaho 83401*

(Received 8 May 2016; accepted 9 August 2016)

The structure of a series of lanthanide iron cobalt perovskite oxides, $R(Fe_{0.5}Co_{0.5})O_3$ (R = Pr, Nd, Sm, Eu, and Gd), have been investigated. The space group of these compounds was confirmed to be orthorhombic *Pnma* (No. 62), $Z = 4$. From Pr to Gd, the lattice parameter a varies from 5.466 35(13) Å to 5.507 10(13) Å, b from 7.7018(2) to 7.561 75(13) Å, c from 5.443 38(10) to 5.292 00(8) Å, and unit-cell volume V from 229.170(9) Å^3 to 220.376(9) Å^3, respectively. While the trend of V follows the trend of the lanthanide contraction, the lattice parameter "a" increases as the ionic radius $r(R^{3+})$ decreases. X-ray diffraction (XRD) and transmission electron microscopy confirm that Fe and Co are disordered over the octahedral sites. The structure distortion of these compounds is evidenced in the tilt angles θ, ϕ, and ω, which represent rotations of an octahedron about the pseudocubic perovskite $[110]_p$, $[001]_p$, and $[111]_p$ axes. All three tilt angles increase across the lanthanide series (for R = Pr to R = Gd: θ increases from 12.3° to 15.2°, ϕ from 7.5° to 15.8°, and ω from 14.4° to 21.7°), indicating a greater octahedral distortion as $r(R^{3+})$ decreases. The bond valence sum for the sixfold (Fe/Co) site and the eightfold R site of $R(Fe_{0.5}Co_{0.5})O_3$ reveal no significant bond strain. Density Functional Theory calculations for $Pr(Fe_{0.5}Co_{0.5})O_3$ support the disorder of Fe and Co and suggest that this compound to be a narrow band gap semiconductor. XRD patterns of the $R(Fe_{0.5}Co_{0.5})O_3$ samples were submitted to the Powder Diffraction File. © *2016 International Centre for Diffraction Data*. [doi:10.1017/S088571561600049X]

Key words: $R(Fe_{0.5}Co_{0.5})O_3$ (R = Pr, Nd, Sm, Eu, and Gd), DFT calculations, TEM, crystal structure, X-ray powder diffraction patterns

I. INTRODUCTION

Over the past decade, the need to create a sustainable energy future has resulted in the increasing global interest in research and development on thermoelectric (TE) materials. The efficiency and performance of TE energy conversion is related to the dimensionless figure of merit (ZT) of the TE materials, given by $ZT = S^2\sigma T/\kappa$, where T is the absolute temperature, S is the Seebeck coefficient or TE power, σ is the electrical conductivity, and k is the thermal conductivity (Nolas *et al.*, 2001). Only a small number of materials have been found to have practical industrial applications and all of those exhibit ZT values around or below 1.0. Optimization of the ZT values is not straightforward because S, σ, and κ are interrelated. Reports that relatively high ZT values are possible in both thin film and bulk forms have revitalized interest in development of TE materials (Tritt, 1996; Ghamaty and Eisner, 1999; Venkatasubramanian *et al.*, 2001; Hsu *et al.*, 2004; Dresselhaus *et al.*, 2007).

The stability of metal oxides at high temperature has made these materials highly relevant to waste heat conversion applications. For example, cobaltates that include $La_{1-x}A_xCoO_3$ (A = Pb, Na) (He *et al.*, 2006), $NaCoO_x$ (Terasaki *et al.*, 1997), $Ca_2Co_3O_6$ (Mikami *et al.*, 2003; Mikami and Funahashi, 2005), $Ca_3Co_4O_9$ (Masset *et al.*, 2000; Mikami *et al.*, 2002; Grebille *et al.*, 2004; Hu *et al.*, 2005), $Bi_2Sr_2Co_2O_x$ (Shin and Murayama, 2000; Wang *et al.*, 2009), and $Ba_2Ho(Cu_{3-x}Co_x)O_{6+x}$ (Wong-Ng *et al.*, 2009) combine large Seebeck coefficients and relatively low thermal conductivities. Consequently in recent years, considerable research has been conducted on oxide TEs, including phase diagram studies of ternary oxide systems using CaO and Co_3O_4 as two of the end members (Wong-Ng *et al.*, 2010, 2011, 2013, 2014).

The lanthanide-containing double perovskite iron cobaltates may also offer desirable TE properties. This paper describes the structure and X-ray reference pattern determination of the $R(Fe_{0.5}Co_{0.5})O_3$ (R = Pr, Nd, Sm, Eu, and Gd) system. We used density functional theory (DFT) calculations to investigate the structural stability of $Pr_2(FeCo)O_6$ in comparison with experimental data, followed by electronic density of

[a]Author to whom correspondence should be addressed. Electronic mail: winnie.wong-ng@nist.gov

https://doi.org/10.1017/S088571561600049X Published online by Cambridge University Press

states (DOS) calculations to reveal its electrical properties. Since X-ray diffraction (XRD) is a non-destructive technique for phase identification, XRD patterns are especially important for phase characterization; therefore another goal of this investigation was to determine the experimental patterns for $R(Fe_{0.5}Co_{0.5})O_3$, and to make them widely available through submission to the Powder Diffraction File (PDF, 2016).

II. EXPERIMENTAL

A. Sample preparation

Samples were prepared from stoichiometric amounts of R_2O_3 Co_3O_4, and Fe_2O_3 (all raw materials are 99.9% pure) using solid-state high-temperature techniques. The starting samples were mixed, pelletized, and heat treated in air at 750 °C for 1 day and subsequently annealed at 950 °C for 15 h, 980 °C for 80 h with intermediate grindings, and 1050 °C for 60 h with intermediate grindings. During each heat treatment, the samples were furnace cooled. The heat treatment process was repeated until no further changes could be detected in the X-ray powder diffraction patterns.

B. X-ray Rietveld refinements and powder reference patterns

X-ray powder diffraction patterns of $R(Fe_{0.5}Co_{0.5})O_3$ powders were measured using a Bruker D2 Phaser diffractometer equipped with a LynxEye position-sensitive detector (certain commercial equipment, instruments, or materials are identified in this paper in order to specify the experimental procedure adequately. Such identification is not intended to imply recommendation or endorsement by the National Institute of Standards and Technology, nor is it intended to imply that the materials or equipment identified are necessarily the best available for the purpose). Patterns were measured (Cu$K\alpha$ radiation, 30 kV, 10 mA, 0.6 mm divergence slit, 2.5° Soller slits, 3 mm scatter screen height) from 5° to 130° 2θ in 0.020 214 4° steps, counting for 1 s step^{-1}. To minimize fluorescence, the lower window of the MCA was changed from its default value of 0.11–0.19 V.

The Rietveld refinement technique (Rietveld, 1969) with the software package GSAS (Larson and von Dreele, 2004) was used to analyze the diffraction patterns of $R(Fe_{0.5}Co_{0.5})O_3$ (R = Pr, Nd, Sm, Eu, and Gd). The structure of La_2FeCoO_6 (PDF 4-13-6526, Karpinsky *et al.*, 2006) reported previously, was used as a starting model for the refinement process. All Fe/Co sites were refined assuming equiatomic occupancies. The constant wavelength Pseudo-Voigt profile function (function #4 with 18 terms) was used for all refinements (Thompson *et al.*, 1987; Finger *et al.*, 1994; Stephens, 1999). GSAS offers a number of different background functions. For each of these functions, the number of terms to be used is adjustable. The more number of terms, the more complex is the shape that can be fit. In theory, each function will have advantages under different circumstances. In general, the Shifted Chebyschev (type #1) is preferable to the others for the vast majority of Rietveld refinements. In this work, background correction was performed using the GSAS background function #1 with six terms, and an absorption/surface roughness correction was applied using function #3.

Reference patterns were obtained with a Rietveld pattern decomposition technique. Using this technique, the reported peak positions were derived from the extracted integrated intensities, and positions calculated from the lattice parameters. When peaks are not resolved at the resolution function, the intensities are summed, and an intensity-weighted d-spacing is reported.

C. Transmission electron microscopy (TEM)

Samples of $Pr_2(Fe_{0.5}Co_{0.5})O_3$ for TEM were prepared by dispersing the crushed powder on a lacey-carbon-coated copper grid. Electron diffraction and imaging were performed using a TEM operated at 300 kV.

D. Bond valence sum (V_b) calculations

The bond valence sum values, V_b, for the R, Fe, and Co sites were calculated using the Brown-Altermatt empirical expression (Brown and Altermatt, 1985; Breese and O'Keeffe, 1991). The V_b of an atom i is defined as the sum of the bond valences v_{ij} of all the bonds from atoms i to atoms j. The most commonly adopted empirical expression for the bond valence v_{ij} as a function of the interatomic distance d_{ij} is $v_{ij} = \exp^{[(R_0 - d_{ij})/B]}$. The parameter, B, is commonly taken to be a "universal" constant equal to 0.37 Å. The values for the reference distance R_0 for Fe–O, Co–O, Pr–O, Nd–O, Sm–O, Eu–O, and Gd–O are 1.759, 1.70, 2.135, 2.117, 2.088, 2.076, and 2.065, respectively (Brown and Altermatt, 1985; Breese and O'Keeffe, 1991). For sites shared by several species, the resulting bond-valence sum (BVS) is the weighted sum using the site occupancy.

E. Computation methods

Structural optimization and electronic structure calculations of $Pr_2(FeCo)O_6$ were performed using Vienna *ab initio* simulation package (VASP) (Kresse and Furthmuller, 1996), based on DFT. The generalized gradient approximation with the Perdew–Becke–Erzenhof parameterization was used to estimate the exchange–correlation functional (Perdew *et al.*, 1996). DFT + U calculations were also implemented using a cutoff energy of 400 eV for the expansion of the plane-wave basis set within the projector augmented wave formalism (Blőchl, 1994; Kresse and Joubert, 1999). Perovskite structure relaxation, according to the conjugate-gradient algorithm, was converged with the residual Hellman–Feynman forces of <0.01 eV Å^{-1}. For the electronic structure calculations, we applied the GGA + U scheme of Liechtenstein *et al.* (1995) with a Hubbard U effective on-site coulomb interaction to the f-orbitals of Pr and d-orbitals of Fe and Co: U_{Pr} = 18 eV, U_{Fe} = 18 eV, and U_{Co} = 12 eV. The DFT + U method could overcome the band gap underestimation by a traditional DFT method. We also optimized the U values for Pr, Fe, and Co and the k-mesh sampling in the Brillouin zone with DOS convergence tests. The DFT + U method is the common and reliable method to calculate electronic structure for a wide range of materials with highly-correlated elements.

In order to model disorder structures and accommodate 0.5 occupancy factor of Fe and Co and their randomness on the B sites, we used 1 × 1 × 1, 2 × 1 × 1, and 2 × 2 × 1 cells of $Pr_2(FeCo)O_6$ with different atomic arrangements of Fe

https://doi.org/10.1017/S088571561600049X Published online by Cambridge University Press

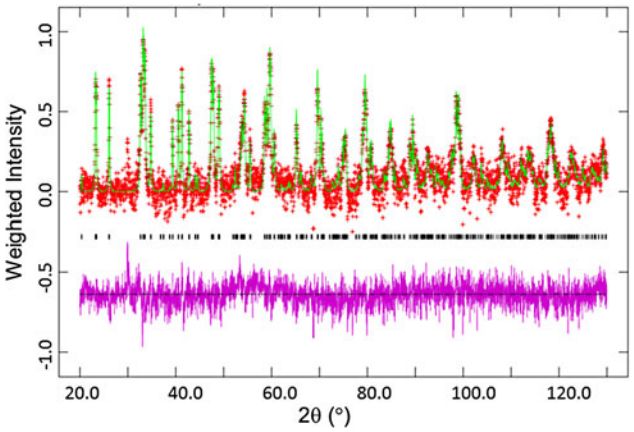


Figure 1. Observed (crosses), calculated (solid line), and difference XRD patterns (bottom) for $Nd(Fe_{0.5}Co_{0.5})O_3$ by the Rietveld analysis technique. The difference pattern is plotted at the same scale as the other patterns. The vertical scale is not the raw intensity, but the weighted intensity; this plot emphasizes the fit to the weaker peaks. The peak at 29.6° results from CuK_β contamination.

and Co for comparison. Note that the occupancies of Fe and Co atoms in different cells remain equivalent. To further study the electrical properties of $Pr_2(FeCo)O_6$ compound, we applied the DFT + U approach to calculate DOS with more dense k-mesh sampling.

III. RESULTS AND DISCUSSION

A. XRD and TEM studies

Figure 1 displays the results of Rietveld refinements for $Nd_2(Fe_{0.5}Co_{0.5})O_3$. The observed (crosses), calculated (solid line), and difference XRD patterns (bottom) as determined by the Rietveld analysis, are shown. The difference pattern is plotted on the same scale as other patterns. The tick marks indicate the calculated peak positions. Since Fe and Co fluoresce when illuminated with Cu radiation, even with attempts to reduce the fluorescence by adjusting the analyzer electronics settings, some fluorescence still remains. Figure 1 is a weighted least-squares plot, to highlight the weak reflections (Larson and von Dreele, 2004). Table I gives the refinement results. Table II tabulates the lattice parameters and calculated density D_x. As expected, the D_x values increase as the size of ionic radius, $r(R^{3+})$ (Shannon, 1976), decreases. The atomic coordinates and displacement parameters are given in Table III. Table IV summarizes the bond distances, selected bond angles, and BVS values.

$R(Fe_{0.5}Co_{0.5})O_3$ phases reportedly acquire orthorhombic *Pnma* (No. 62) symmetry (Karpinsky *et al.*, 2006), as

TABLE I. Rietveld refinement results (R_p, R_{wp}, and χ^2) of $R(Fe_{0.5}Co_{0.5})O_3$ (R = Pr, Nd, Sm, Eu, and Gd), *Pnma* (No. 62), $Z = 2$.

Composition	R_{wp}	R_p	χ^2
$Pr(Fe_{0.5}Co_{0.5})O_3$	0.0749	0.0579	1.35
$Nd(Fe_{0.5}Co_{0.5})O_3$	0.0777	0.0592	1.38
$Sm(Fe_{0.5}Co_{0.5})O_3$	0.0687	0.0539	1.23
$Eu(Fe_{0.5}Co_{0.5})O_3$	0.0800	0.0618	1.43
$Gd(Fe_{0.5}Co_{0.5})O_3$	0.0634	0.0490	1.25

determined by the combined anti-phase and in-phase octahedral rotations, which can be described as $a^-a^-c^+$ using Glazer's notation. The unit-cell volume (Figure 2) for $R(Fe_{0.5}Co_{0.5})O_3$ increases monotonically with the increasing size of $r(R^{3+})$, from Gd to Pr, respectively. The volume increase is mainly due to the larger b and c lattice parameters, although the magnitude of the a-parameter maintains an opposite trend (Table II). This trend implies that the twisting of the [(Fe/Co)O_6] octahedra in $R(Fe_{0.5}Co_{0.5})O_3$ has a larger influence on the magnitude of the a-cell parameter, while that of the size of eight-coordination polyhedra, [RO_8], has a stronger effect on b and c.

Electron diffraction patterns (Figure 3) feature sharp superlattice reflections at ½*ooo* and ½*ooe* locations ("*o*" and "*e*" refer to the odd and even reflection indexes, respectively, for a perovskite unit cell with $a_0 \approx 4$ Å). These superlattice reflections are consistent with the presence of both anti-phase and in-phase octahedral rotations. All the reflections are indexable according to the unit cell $\sqrt{2}a_0 \times 2a_0 \times \sqrt{2}a_0$ and reflection conditions $hk0$ $h = 2n$ agree with the *Pnma* (No. 62) space group, which is expected for the $a^-a^-c^+$ octahedral tilting. No hints of Fe/Co ordering could be observed. For example, a common rock-salt-type ordering of these cations would yield 110 reflections, which, however, are notably absent in the present diffraction patterns. These observations agree with Galasso and Pyle (1963a, 1963b) and Blasse (1965) which suggest weakening of long-range B-site order with decreasing mismatch between the ionic radii of B-cations sharing the same crystallographic site, as encountered for Fe and Co.

Figures 4 and 5 illustrate the structure of $R(Fe_{0.5}Co_{0.5})O_3$. In orthorhombic $R_2M_2O_6$ ("*M*" is used to represent the mixed site Co/Fe), there are two distinct *M*–O–*M* angles (*M*–O4–*M* and *M*–O5–*M*) that relate neighboring octahedra. The *M*–O4–*M* angle (Figure 5) and the *M*–O5–*M* angles (Figure 4) which both deviate from the ideal value of 180° reflect the degree of octahedral tilting. The three tilt angles θ, ϕ, and ω which follow the notation of Zhao *et al.* (1993a, 1993b) to represent rotations of octahedral about the pseudocubic $[110]_p$,

TABLE II. Unit-cell parameters of $R(Fe_{0.5}Co_{0.5})O_3$ (R = Pr, Nd, Sm, Eu, and Gd) [*Pnma* (No. 62), $Z = 2$, D_x refers to calculated density]. Uncertainties refer to standard deviation. $r(R^{3+})$ (Å) is the ionic radius for R (VIII coordination).

Compounds	a (Å)	b (Å)	c (Å)	V (Å^3)	D_x (g cm^{-3})	r (R^{3+})
$La(Fe_{0.5}Co_{0.5})O_3$ (Karpinsky *et al.* (2006)	5.4351(8)	7.7021(1)	5.4854(8)	229.63	7.066	1.16
$Pr(Fe_{0.5}Co_{0.5})O_3$	5.466 35(13)	7.7018(2)	5.443 38(10)	229.170(9)	7.139	1.126
$Nd(Fe_{0.5}Co_{0.5})O_3$	5.4684(3)	7.6746(3)	5.4126(2)	227.16(2)	7.299	1.109
$Sm(Fe_{0.5}Co_{0.5})O_3$	5.4963(2)	7.6205(2)	5.355 56(10)	224.313(11)	7.574	1.079
$Eu(Fe_{0.5}Co_{0.5})O_3$	5.5125(3)	7.6052(3)	5.3325(2)	223.56(2)	7.646	1.066
$Gd(Fe_{0.5}Co_{0.5})O_3$	5.507 10(13)	7.561 75(13)	5.292 00(8)	220.376(9)	7.916	1.053

https://doi.org/10.1017/S088571561600049X Published online by Cambridge University Press

TABLE III. Atomic coordinates and isotropic displacement factors for $R(Fe_{0.5}Co_{0.5})O_3$; [Pnma (No. 62), $Z = 2$, D_x refers to calculated density]. SOF stands for site occupancy factor. Uncertainties refer to standard deviation.

Atom	x	y	z	SOF.	U_{iso}	Wychoff Sym.
(i) $R = Pr$						
Pr1	0.4638(2)	0.25	0.0071(7)	1.0	0.0141(3)	4*c*
Fe_2/Co_3	0.0	0.0	0.0	0.5	0.0128(6)	4*a*
O4	0.517(2)	0.25	0.575(3)	1.0	0.012(2)	4*c*
O5	0.218(2)	0.049(2)	0.284(2)	1.0	0.012(2)	8*d*
(ii) $R = Nd$						
Eu1	0.4587(3)	0.25	0.0082(7)	1.0	0.0093(6)	4*c*
Fe_2/Co_3	0.0	0.0	0.0	0.5	0.0123(7)	4*a*
O4	0.521(3)	0.25	0.574(3)	1.0	0.01	4*c*
O5	0.218(3)	0.051(2)	0.283(3)	1.0	0.01	8*d*
(iii) $R = Sm$						
Eu1	0.4470(3)	0.25	0.0123(4)	1.0	0.0119(4)	4*c*
Fe_2/Co_3	0.0	0.0	0.0	0.5	0.0109(9)	4*a*
O4	0.528(3)	0.25	0.590(3)	1.0	0.012(3)	4*c*
O5	0.204(2)	0.044(2)	0.298(2)	1.0	0.012(3)	8*d*
(iv) $R = Eu$						
Eu1	0.4440(3)	0.25	0.0135(5)	1.0	0.0093(6)	4*c*
Fe_2/Co_3	0.0	0.0	0.0	0.5	0.0141(11)	4*a*
O4	0.534(3)	0.25	0.590(3)	1.0	0.01	4*c*
O5	0.204(2)	0.053(2)	0.298(2)	1.0	0.01	8*d*
(v) $R = Gd$						
Eu1	0.4440(3)	0.25	0.0135(5)	1.0	0.0093(6)	4*c*
Fe_2/Co_3	0.0	0.0	0.0	0.5	0.0141(11)	4*a*
O4	0.534(3)	0.25	0.590(3)	1.0	0.01	4*c*
O5	0.204(2)	0.053(2)	0.298(2)	1.0	0.01	8*d*

$[001]_p$, and $[111]_p$ axes, respectively, are shown in Table IVb. All the three tilt angles increase for $R = Pr$ to $R = Gd$: θ from 12.268° to 15.148°, ϕ from 7.522° to 15.776°, and ω from 14.360° to 21.737°. This increase across the lanthanide series indicates a greater octahedral distortion as the size of R decreases.

The Goldschmidt geometrical tolerance factor (t) is a criterion for the stability and distortion of perovskite structures. It can also be used to calculate the compatibility of an ion with a crystal structure. The tolerance factor t is defined as $t = \langle r_A + r_O \rangle / \sqrt{2}\langle r_B + r_O \rangle$ (Goldschmidt, 1926), where r_A, r_B, and r_O represent the ionic radii of A-cations, B-cations, and oxygen, respectively. In the ideal cubic structure with $t = 1$, the unit-cell parameter a can be described as $a = \sqrt{2}\langle r_A + r_O \rangle = 2\langle r_B + r_O \rangle$. As t approaches 1, the structure is expected to become less distorted; with $t < 1$ the distortion is accommodated by the cooperative rotations of the $[BO_6]$ octahedra, resulting in a lower symmetry. In $R(Fe_{0.5}Co_{0.5})O_3$, the coordination

TABLE IV. Bond distances and bond-valence sum (BVS) values for $R(Fe_{0.5}Co_{0.5})O_3$ (R = Pr, Nd, Sm, Eu, and Gd), M = Co/Fe. If more than one atom types occupy the same site, the resulting BVS is the weighted sum of each site occupancy. Uncertainties refer to standard deviation.

		Distances (Å)				
Atom	Atom	Pr	Nd	Sm	Eu	Gd
(a) Bond distances (Å)						
R	O4	2.37(2)	2.37(2)	2.303(13)	2.315(14)	2.369(13)
	O4	2.484(13)	2.437(15)	2.367(15)	2.32(2)	2.251(13)
	O5	2.54(2)×2	2.51(2)×2	2.567(14)×2	2.512(15)×2	2.509(12)×2
	O5	2.79(2)×2	2.78(2)×2	2.651(14)×2	2.698(15)×2	2.662(11)×2
	O5	2.369(10)×2	2.372(11)×2	2.343(9)×2	2.304(10)×2	2.281(8)×2
M	O4	1.970(4)×2	1.964(4)×2	1.972(3)×2	1.970(3)×2	1.948(3)×2
	O5	1.986(5)×2	1.979(5)×2	1.979(4)×2	1.988(5)×2	2.002(4)×2
	O5	1.978(5)×2	1.978(5)×2	1.982(4)×2	1.997(5)×2	1.984(4)×2
(b) Estimated tilt angles θ, ϕ, and ω (°)						
Site	Pr	Nd	Sm	Eu	Gd	
θ	12.3	12.2	14.9	15.2	15.2	
ϕ	7.5	7.4	10.6	15.8	15.8	
ω	14.4	14.3	18.2	21.8	21.7	
(c) BVS, M = Co/Fe						
R	2.992	2.954	3.018	3.109	3.161	
M	3.076	3.111	3.078	3.019	3.081	

https://doi.org/10.1017/S088571561600049X Published online by Cambridge University Press

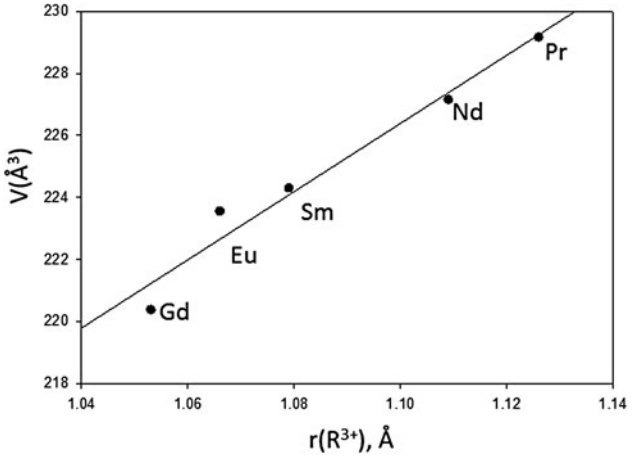


Figure 2. Plot of unit-cell volume, V, of $R(Fe_{0.5}Co_{0.5})O_3$ (R = Pr, Nd, Sm, Eu, and Gd) vs. $r(R^{3+})$. A monotonic decrease of V is observed which follows the trend of lanthanide contraction.

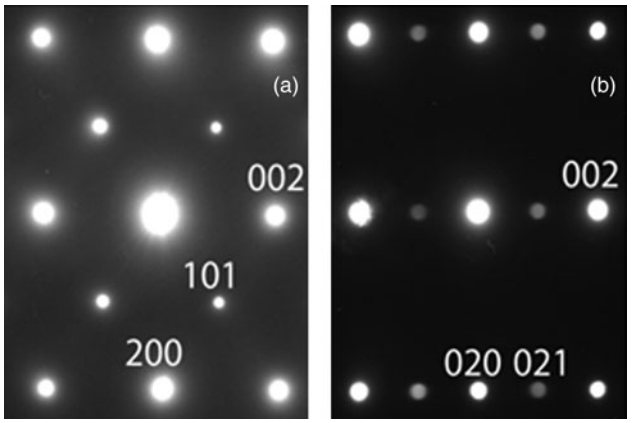


Figure 3. Electron diffraction patterns for $Pr(Fe_{0.5}Co_{0.5})O_3$ in [100] (a) and [001] (b) zone axis orientations of the orthorhombic $\sqrt{2}a_0 \times 2a_0 \times \sqrt{2}a_0$ unit cell. The superlattice reflections 011 (½*ooo* in the cubic perovskite indexes) and 210 (½*ooe*) arise because of octahedral rotations; the intensities of the latter are dominated by contributions from the antiparallel Pr displacements that accompany the octahedral tilting. The 110 reflections are absent consistent with the *Pnma* space group and disordered Co and Fe.

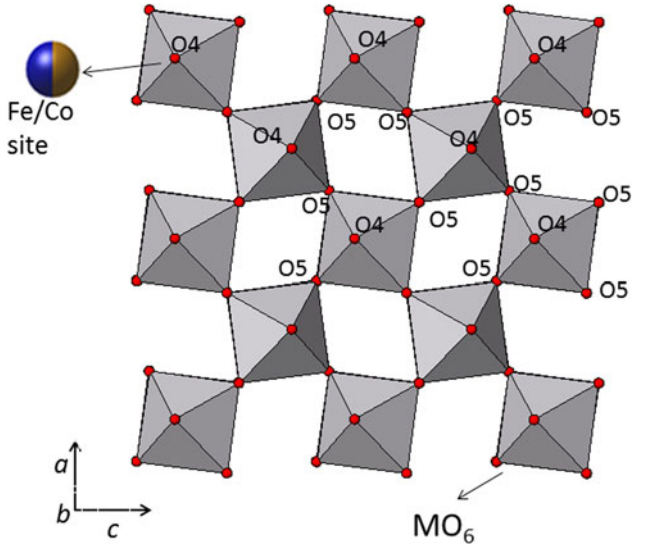


Figure 4. Crystal structure of $R(Fe_{0.5}Co_{0.5})O_3$ (R = Pr, Nd, Sm, Eu, and Gd) based on X-ray powder data, showing the unit-cell outline, labeling of various atoms, and the coordination environment of the distorted $[(Co, Fe)O_6]$ octahedra view along the *b*-axis. R atoms are not shown for clarity.

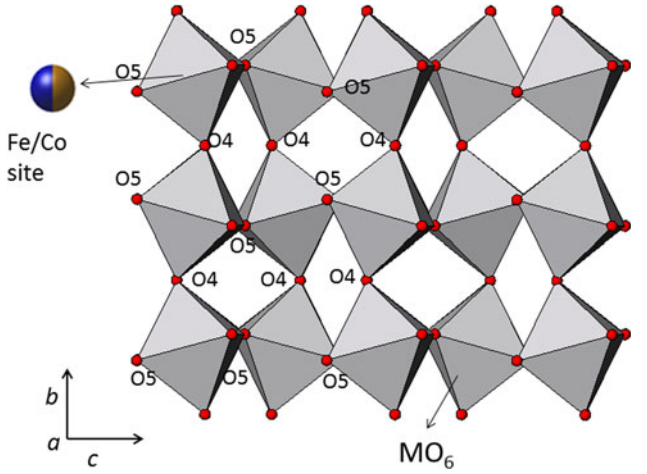


Figure 5. Crystal structure of $R(Fe_{0.5}Co_{0.5})O_3$ (R = Pr, Nd, Sm, Eu, and Gd) based on X-ray powder data, showing the unit-cell outline, labeling of various atoms, and the coordination environment of the distorted $[(Co, Fe)O_6]$ octahedra view along the *a*-axis. *R* atoms are not shown for clarity.

TABLE V. Calculated structure parameters by DFT for $Pr(Fe_{0.5}Co_{0.5})O_3$ compound. Error % refers to the difference between calculated and experimental volume data.

$Pr_2(FeCo)O_6$					
Superlattice	*a* (Å)	*b* (Å)	*c* (Å)	Volume (Å^3)	Error (%)
Structure I	5.528 34	7.566 86	5.282 27	220.96	3.6
Structure II	5.641 76	7.498 77	5.208 69	220.36	3.8
Structure III	5.532 63	7.5626	5.301 41	221.81	3.2
Disordered					
Structure I	5.492 58	7.487 33	5.4624	224.64	1.9
Structure II	5.614 38	7.494 99	5.462 66	229.87	0.3
Experimental	5.466 35 (13)	7.7018 (2)	5.443 38 (10)	229.170 (9)	

https://doi.org/10.1017/S088571561600049X Published online by Cambridge University Press

TABLE VI. Calculated bond distances by DFT for $Pr(Fe_{0.5}Co_{0.5})O_3$ compound.

Bonds lengths	Experimental (Å)	Disordered Structure II (Å)
Pr		
O4	2.37(2)	2.292 49
O4	2.484(13)	2.313 71
O5	2.54(2)×2	2.543 40, 2.530 43
O5	2.79(2)×2	2.757 60, 2.637 64
O5	2.369(10)×2	2.281 97, 2.288 87
Co/Fe		
O4	1.970(4)×2	1.959 03, 1.958 17
O5	1.986(5)×2	2.091 83, 2.051 89
O5	1.978(5)×2	2.022 68, 1.963 38

number (c.n.) is 8 for R^{3+} sites and 6 for the Fe^{3+}/Co^{3+} sites. The experimental *R*–O and Fe/Co–O values are used to compute the *t* values. As $r(R^{3+})$ decreases across the lanthanide series, so do the *t* values. The *t* values for $R(Fe_{0.5}Co_{0.5})O_3$, as R = Pr, Nd, Sm, Eu, and Gd are 0.889, 0.885, 0.869, 0.863, and 0.857, respectively. These *t* values fall in the range of Goldschmidt "orthorhombic/rhombohedral" structure type, 0.71–0.90 (Goldschmidt, 1926).

The BVS values (Table IVc) for the R^{3+} site (ranging from 2.99 to 3.162) and for the (Fe/Co)–O site (3.019–3.111) in $R(Fe_{0.5}Co_{0.5})O_3$ imply near strain-free situation ($V_b > 3.0$, the ideal valence value). Indeed, octahedral tilting in these structures relieves bond strain.

B. Structural stability and electrical properties

Table V shows the structural data derived for different superlattices and disordered structures for $Pr(Fe_{0.5}Co_{0.5})O_3$. Through the total energy minimization approach a disordered $Pr(Fe_{0.5}Co_{0.5})O_3$ structure is more stable than its ordered variants. Disordered Structure II has lattice parameters $a = 5.61$, $b = 7.50$, and $c = 5.46$ Å. Its unit-cell volume is 229.87 $Å^3$. We found that the calculated lattice parameter *c* and volume agree well with the experimental data, while the lattice parameters *a* and *b* are slightly different from the experimental values by <3%. This difference could be attributed to the fact that the experimental lattice parameters are measured as the average values of the unit cells on a macro scale, whereas DFT calculations present the local structure features on a much smaller atomic scale. Table VI compares the calculated and experimental Pr–O and Fe(Co)–O bond distances. In general, the Pr–O bonds are longer than the Fe(Co)–O bonds. DFT calculations indicate that the disorder of Fe and Co leads to larger lattice parameters and unit-cell volume. Expanding the cell size provides more options for the ordered atomic arrangement of Fe and Co on the B sites. Starting from a 1 × 1 × 1 unit cell, we double the lattice parameters *a* and *b*, and estimated total energy/atom for each supercell. Disordered Structure II has a 2 × 2 × 1 cell and completely random arrangement of Fe and Co atoms on the B sites (Figure 6). Its total energy/atom is slightly lower (by ~0.42%, i.e. more negative) than that for Disordered Structure I with a 2 × 1 × 1 cell. This result implies that the random occupancy of the B sites is energetically favorable in the $Pr(Fe_{0.5}Co_{0.5})O_3$ compound.

Figure 7 shows a small band gap near the Fermi energy E_F. $Pr_2(FeCo)O_6$ is a semiconductor with a band gap of

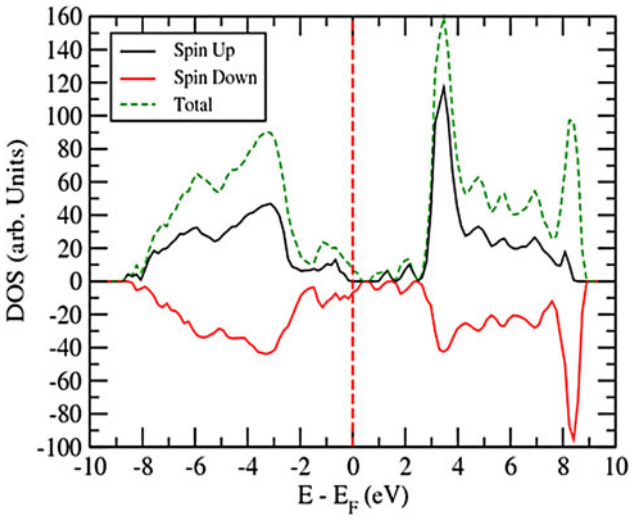


Figure 7. DOS for $Pr(Fe_{0.5}Co_{0.5})O_3$ with a band gap of $E_g \approx 0.43$ eV. E_f refers to Fermi energy.

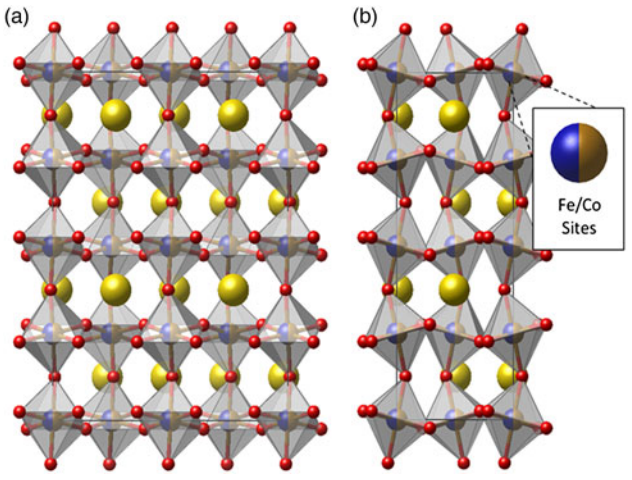


Figure 6. (a) Front view and (b) side view of the 2 × 2 × 1 supercell of Pr $(Fe_{0.5}Co_{0.5})O_3$, including disordered B-sites with 50–50 occupation of Fe and Co.

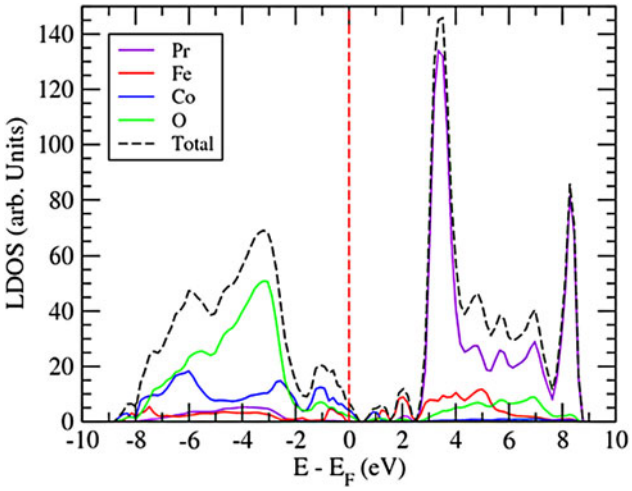


Figure 8. Local DOS for $Pr(Fe_{0.5}Co_{0.5})O_3$ projected on Pr, Fe, Co, and O atoms in comparison with total DOS.

https://doi.org/10.1017/S088571561600049X Published online by Cambridge University Press

TABLE VII. X-ray powder pattern for $Sm(Fe_{0.5}Co_{0.5})O_3$ [*Pnma* (No. 62), $Z = 2$, $a = 5.4963(2)$ Å, $b = 7.6205(2)$ Å, $c = 5.355\,56(10)$ Å, $V = 224.313(11)$ Å^3, $D_x = 7.574$ g cm^{-3}]. The symbols "*M*" and "+" refer to peaks containing contributions from two and more than two reflections, respectively. The particular peak that has the strongest intensity in the entire pattern is assigned an intensity of 999 and other lines are scaled relative to this value. The *d*-spacing values are calculated values from refined lattice parameters, and "*I*" represents integrated intensity values.

d	*I*	*h*	*k*	*l*	*d*	*I*	*h*	*k*	*l*	*d*	*I*	*h*	*k*	*l*
4.3817	10	0	1	1	3.8357	161	1	0	1	3.8103	86	0	2	0
3.4262	125	1	1	1	2.7481	209	2	0	0	2.7032	999	1	2	1
2.6778	327	0	0	2	2.5852	76	2	1	0	2.2955	27	1	1	2
2.2289	66	2	2	0	2.1909	147	0	2	2	2.1179	57	1	3	1
1.9179	243	2	0	2	1.9051	155	0	4	0	1.8654	48	2	3	0
1.8599	100	2	1	2	1.7616	15	2	3	1	1.7473	18	1	3	2
1.7131	33	2	2	2	1.7063	49	1	4	1	1.6979	32	1	0	3
1.6903	148	3	1	1	1.6572	41	1	1	3	1.5779	138	3	2	1
1.5657	89	2	4	0	1.5513	440	0	4	2 M	1.5513	440	1	2	3 M
1.5306	42	2	3	2	1.4971	10	2	0	3	1.4318	61	3	3	1
1.3517	148	4	1	0 M	1.3517	148	2	4	2 M	1.3389	43	0	0	4
1.2823	7	1	1	4	1.2675	18	1	4	3	1.2610	33	3	1	3
1.2122	38	3	2	3	1.2086	16	4	3	0	1.2057	1561	6	1+	
1.1932	19	2	5	2	1.1889	20	2	1	4	1.1476	10	0	6	2
1.1446	34	3	5	1	1.1421	37	3	3	3	1.1144	16	4	4	0
1.1016	46	4	3	2	1.0954	45	0	4	4	1.0877	20	2	3	4
1.0662	42	5	1	1	1.0513	12	1	0	5	1.0289	16	4	4	2
1.0245	25	3	6	1	1.0205	18	4	5	0	1.0176	48	2	4	4
1.0170	69	1	6	3	1.0135	76	1	2	5	0.9914	38	5	3	1
0.9795	23	3	5	3	0.9536	25	4	5	1	0.9526	14	0	8	0
0.9514	36	4	1	4	0.9468	10	2	7	2	0.9446	12	2	5	4
0.9291	31	5	1	3	0.9219	19	3	7	1	0.9205	14	1	4	5
0.9179	22	3	1	5	0.9011	22	3	6	3	0.9000	25	2	8	0
0.8986	40	3	2	5	0.8973	65	0	8	2 M	0.8973	65	4	3	4 M
0.8926	13	0	0	6	0.8795	27	5	5	1	0.8783	26	5	3	3
0.8689	17	3	3	5	0.8614	46	6	3	0 M	0.8614	46	6	1	2 M
0.8566	17	4	4	4	0.8532	66	4	7	0 M	0.8532	66	2	8	2 M

$E_g \approx 0.43$ eV (As mentioned earlier, DFT + U method was applied to overcome the band gap underestimation by traditional DFT method. We also optimized the *U* values for Pr, Fe, and Co and the *k*-mesh sampling in the Brillouin zone with DOS convergence tests.) The spin-up and spin-down densities are slightly asymmetric and favor the spin-down configuration below the Fermi energy E_f, causing a small net magnetism. As shown in Figure 8, the local DOS is projected onto individual Pr, Fe, Co, and O atoms to reveal their contributions to the electrical properties of the compound. O and Co provide the main contributions to the total DOS below E_f, while Pr and Fe dominate above E_f between 0 and 2.5 eV. Intense orbital hybridization around E_f also gives evidence that covalency plays an important role in the perovskite bonding characteristics.

C. Reference XRD patterns

An example of the reference pattern of $Sm(Fe_{0.5}Co_{0.5})O_3$ is shown in Table VII. In this pattern, the symbols "*M*" and "+" refer to the peaks that contain contributions of 2 and more than 2 reflections, respectively. The strongest peak in the pattern is assigned an intensity of 999 and other lines are scaled relative to this value. The *d*-spacing values are calculated values from refined lattice parameters. The intensity values reported are integrated intensities (rather than peak heights) calculated from corresponding profile parameters as reported in Table VII. For peaks containing more than one reflection that can still be resolved , intensity-weighted calculated *d*-spacing, along with the observed integrated intensity and the *hkl* indices of both peaks (for "*M*"), or the *hkl* indices of the strongest peak (for "+") are used. For peaks that are not resolved within the instrumental resolution, the intensity-weighted average *d*-spacing and the summed integrated intensity value are used. In the case of a cluster, unconstrained profile fits often reveal the presence of multiple peaks, even when they are closer than the instrumental resolution. In this situation, both *d*-spacing and intensity values are reported independently. All patterns have been submitted for inclusion in the Powder Diffraction File (PDF).

IV. SUMMARY

Crystal structure and powder diffraction reference patterns of the perovskite $R(Fe_{0.5}Co_{0.5})O_3$ (R = Pr, Nd, Sm, Eu, and Gd) compounds have been determined and the latter have been submitted to the PDF. The Co/Fe sites in this double perovskite series are disordered, as supported by both TEM and DFT calculations. Octahedral tilting was observed in these compounds with the tilt angles (distortion) increasing as r (R^{3+}) decreases; the tilting relieves the *R*–O bond strain. DFT + *U* calculations for $Pr(Fe_{0.5}Co_{0.5})O_3$ indicated it to be a narrow band gap semiconductor, which will be validated by experiment in the future.

SUPPLEMENTARY MATERIAL

To view supplementary material for this article, please visit http://dx.doi.org/10.1017/S088571561600049X.

https://doi.org/10.1017/S088571561600049X Published online by Cambridge University Press

ACKNOWLEDGEMENT

ICDD is acknowledged for Grant-in-Aid assistance for the project.

Blasse, G. (**1965**). "New compounds with perovskite-like structures," J. Inorg. Nucl. Chem. **27**, 993–1003.

Blőchl, P. E. (**1994**). "Projector augmented-wave method," Phys. Rev. B **50**, 17953.

Brese, N. E. and O'Keeffe, M. (**1991**). "Bond-valence parameters for solids," Acta Crystallogr. B **47**, 192–197.

Brown, I. D. and Altermatt, D. (**1985**). "Bond-valence parameters obtained from a systematic analysis of the inorganic crystal structure database," Acta Crystallogr. B **41**, 244–247.

Dresselhaus, M. S., Chen, G., Tang, M. Y., Yang, R. G., Lee, H., Wang, D. Z., Ren, Z. F., Fleurial, J. P., and Gogna, P. (**2007**). "Enhanced thermopower in PbSe nanocrystal quantum dot superlattices," Adv. Mater. **19**, 1043–1053.

Finger, L. W., Cox, D. E., and Jephcoat, A. P. (**1994**). "A correction for powder diffraction peak asymmetry due to axial divergence", J. Appl. Crystallogr. **27**, 892–900.

Galasso, F. and Pyle, J. (**1963a**). "Ordering in compounds of the $A(B_{0\ 33}Ta_{0\ 67})O_3$ type," Inorg. Chem. **2**, 482–484.

Galasso, F. and Pyle, J. (**1963b**). "Preparation and study of ordering in $A(B_{0\ 33}Nb_{0\ 67})O_3$ perovskite-type compounds," J. Phys. Chem. **67**, 1561–1562.

Ghamaty, S. and Eisner, N. B. (**1999**). "Development of quantum well thermoelectric films," in *Proceedings of the 18th International Conference on Thermoelectrics*, Baltimore, MD, pp. 485–488.

Goldschmidt, V. M. (**1926**). "Die Gesetze der Krystallochemie," Die Naturwissenschaften **14**(21), 477–485.

Grebille, D., Lambert, S., Bourée, F., and Petricek, V. (**2004**). "Contribution of powder diffraction for structure refinements of aperiodic misfit cobalt oxides," J. Appl. Crystallogr. **37**, 823–831.

He, T., Chen, J. Z., Calvarese, T. G., and Subramanian, M. A. (**2006**). "Thermoelectric properties of $La_{1-x}A_xCoO_3$ (A = Pb, Na)," Solid State Sci. **8**, 467–469.

Hsu, K. F., Loo, S., Guo, F., Chen, W., Dyck, J. S., Uher, C., Hogan, T., Polychroniadis, E. K., and Kanatzidis, M. G. (**2004**). "Cubic $AgPb_mSbTe_{2+m}$: bulk thermoelectric materials with high figure of merit," Science **303**, 818–821.

Hu, Y. F., Si, W. D., Sutter, E., and Li, Q. (**2005**). "*In-situ* growth of c-axis-oriented $Ca_3Co_4O_9$ thin films on Si(100)," Appl. Phys. Lett. **86**, 082103.

Karpinsky, D. V., Troyanchuk, I. O., Dobryanskii, V. M., Szymczak, H., and Tovar, M. (**2006**). "Crystal structure and magnetic properties of the $LaCo_{0.5}Fe_{0.5}O_3$ perovskite," Crystallogr. Rep. **51**, 596.

Kresse, G. and Furthmuller, J. (**1996**). "Efficient iterative schemes for ab initio total energy calculations using a plane-wave basis set," Phys. Rev. B **54**, 11169.

Kresse, G. and Joubert, D. (**1999**). "From ultra-soft pseudopotentials to the projector augmented-wave method," Phys. Rev. B **59**, 1758.

Larson, A. C. and von Dreele, R. B. (**2004**). General Structure Analysis System (GSAS), Los Alamos National Laboratory Report LAUR 86–748, Los Alamos, USA.

Liechtenstein, A. I., Anisimov, V. I., and Zaanen, J. (**1995**). "Density-functional theory and strong interactions: orbital ordering in Mott-Hubbard insulators," Phys. Rev. B **52**, R5467.

Masset, A. C., Michel, C., Maignan, A., Hervieu, M., Toulemonde, O., Studer, F., and Raveau, B. (**2000**). "Misfit-layered cobaltite with an anisotropic giant magnetoresistance: $Ca_3Co_4O_9$," Phys. Rev. B **62**, 166–175.

Mikami, M. and Funahashi, R. (**2005**). "The effect of element substitution on high-temperature thermoelectric properties of $Ca_3Co_2O_6$ compounds," J. Solid State Chem. **178**, 1670–1674.

Mikami, H., Itaka, K., Kawaji, H., Wang, Q. J., Koinuma, H., and Lippmaa, M. (**2002**). "Rapid synthesis and characterization of $(Ca_{1-x}Ba_x)_3Co_4O_9$ thin films using combinatorial methods," Appl. Surf. Sci. **197**, 442–447.

Mikami, M., Funahashi, R., Yoshimura, M., Mori, Y., and Sasaki, T. (**2003**). "High-temperature thermoelectric properties of single-crystal $Ca_3Co_2O_6$," J. Appl. Phys. **94**(10), 6579–6582.

Nolas, G. S., Sharp, J., and Goldsmid, H. J. (**2001**). *Thermoelectric: Basic Principles and New Materials Developments* (Springer, New York).

PDF, Powder Diffraction File (**2014**). Produced by International Centre for Diffraction Data, 12 Campus Blvd., Newtown Squares, PA 19073-3273, USA.

Perdew, J. P., Burke, K., and Ernzerhof, M. (**1996**). "Generalized gradient approximation made simple," Phys. Rev. Lett. **77**, 3865.

Rietveld, H. M. (**1969**). "A profile refinement method for nuclear and magnetic structures," J. Appl. Crystallogr. **2**, 65–71.

Shannon, R. D. (**1976**). "Revised effective ionic radii and systematic studies of interatomic distances in halides and chalcogenides," Acta Crystallogr. **A32**, 751–767.

Shin, W. and Murayama, N. (**2000**). "Thermoelectric properties of (Bi, Pb)-Sr-Co-O oxide," J. Mater. Res. **15**(2), 382.

Stephens, P. W. (**1999**) "Phenomenological model of anisotropic peak broadening," J. Appl. Crystallogr. **32**, 281–289.

Terasaki, I., Sasago, Y., and Uchinokura, K. (**1997**). "Large thermoelectric power in $NaCo_2O_4$ single crystals", Phys. Rev. B **56**, 12685–12687.

Thompson, P., Cox, D. E. and Hastings, J. B. (**1987**). "Rietveld refinement of Debye–Scherrer synchrotron X-ray data from Al_2O_3", J. Appl. Crystallogr. **20**, 79–83.

Tritt, T. M. (**1996**). "Thermoelectrics run hot and cold," Science **272**, 1276–1277.

Venkatasubramanian, R., Siivola, E., Colpitts, T. and O'Quinn, B. (**2001**). "Growth of one-dimensional Si/SiGe heterostructures by thermal CVD," Nature **413**, 597–602.

Wang, S., Venimadhav, A., Guo, S., Chen, K., Li, Q., Soukiassian, A., Schlom, D. G., Pan, X. Q., Wong-Ng, W., Vaudin, M. D., Cahill, D. G., and Xi, X. X. (**2009**). "Structural and thermoelectric properties of $Bi_2Sr_2Co_2O_y$ thin films on $LaAlO_3$ (100) and fused silica substrates," Appl. Phys. Lett. **94**, 022110.

Wong-Ng, W., Yang, Z., Hu, Y. F., Huang, Q., Lowhorn, N., Otani, M., Kaduk, J. A., Green, M., and Li, Q. (**2009**). "Thermoelectric and structural characterization of $Ba_2Ho(Cu_{3-x}Co_x)O_{6+x}$," J. Appl. Phys. **105**(6), 63706.

Wong-Ng, W., Liu, G., Martin, J., Thomas, E., Lowhorn, N., and Otani, M. (**2010**). "Phase compatibility of the thermoelectric compounds in the Sr–Ca–Co–O system," J. Appl. Phys., **107**, 033508.

Wong-Ng, W., Luo, T., Tang, M., Xie, M., Kaduk, J. A., Huang, Q., Yang, Y., Tang, M., and Tritt, T. (**2011**). "crystal chemistry and thermoelectric properties of compounds in the Ca–Co–Zn–O system," J. Solid State Chem. **184**(8), 2159.

Wong-Ng, W., Laws, W., and Yan, Y. G. (**2013**). "Phase diagram and crystal chemistry of the La–Ca–Co–O system", Solid State Sci. **17**, 107–110.

Wong-Ng, W., Laws, W., Talley, K. R., Huang, Q., Yan, J., and Kaduk, J. A. (**2014**). "Phase equilibria and crystal chemistry of the CaO–½Nd_2O_3–CoO_z system at 885 °C in air," J. Solid State Chem. **215**, 128–134.

Zhao, Y., Weider, D. J., Parise, J. B., and Cox, D. E. (**1993a**). "Thermal expansion and structural distortion of perovskite – data for $NaMgF_3$ perovskite. Part I," Phys. Earth Planet. Inter. **76**, 1–16.

Zhao, Y., Weider, D. J., Parise, J. B., and Cox, D. E. (**1993b**). "Thermal expansion and structural distortion of perovskite – data for $NaMgF_3$ perovskite. Part II," Phys. Earth Planet. Inter. **76**, 17–34.

https://doi.org/10.1017/S088571561600049X Published online by Cambridge University Press